LETTER

Entanglement of bosonic modes through an engineered exchange interaction

Yvonne Y. Gao[1,2,3,4]*, Brian J. Lester[1,2,3,4]*, Kevin S. Chou[1,2,3], Luigi Frunzio[1,2,3], Michel H. Devoret[1,2,3], Liang Jiang[1,2,3], S. M. Girvin[1,2,3] & Robert J. Schoelkopf[1,2,3]*

Quantum computation presents a powerful new paradigm for information processing. A robust universal quantum computer can be realized with any well controlled quantum system, but a successful platform will ultimately require the combination of highly coherent, error-correctable quantum elements with at least one entangling operation between them[1,2]. Quantum information stored in a continuous-variable system—for example, a harmonic oscillator—can take advantage of hardware-efficient quantum error correction protocols that encode information in the large available Hilbert space of each element[3–5]. However, such encoded states typically have no controllable direct couplings, making deterministic entangling operations between them particularly challenging. Here we develop an efficient implementation of the exponential-SWAP operation[6] and present its experimental realization between bosonic qubits stored in two superconducting microwave cavities. This engineered operation is analogous to the exchange interaction between discrete spin systems, but acts within any encoded subspace of the continuous-variable modes. Based on a control rotation, the operation produces a coherent superposition of identity and SWAP operations between arbitrary states of two harmonic oscillator modes and can be used to enact a deterministic entangling gate within quantum error correction codes. These results provide a valuable building block for universal quantum computation using bosonic modes.

Continuous-variable elements are becoming increasingly prominent components for the realization of robust universal quantum computation. Such systems offer the advantage of more compact information storage and hardware-efficient quantum error correction protocols. Within the circuit quantum electrodynamics (cQED) framework, multiphoton states of superconducting cavities are used to encode continuous-variable quantum information. In particular, three-dimensional (3D) microwave cavities coupled to transmon ancillae have demonstrated long intrinsic lifetimes[7], universal state control[8], and, importantly, have a single dominant error mechanism—single photon loss—that has been successfully mitigated through the use of quantum error correction codes[9]. Furthermore, there are many available bosonic codes[4,10–13], such that the choice of encoding can be optimized for specific applications and local error models. However, up to now, this required developing tailored entangling operations for each encoding[14,15]. A deterministic, codeword-independent entangling gate would be a powerful tool for connecting quantum memories that each harness the strength and flexibility of bosonic encodings in cQED.

A generalized two-mode entangling operation can be enacted by performing a quantum superposition of the identity and SWAP gates. A quantum Fredkin gate (or controlled-SWAP operation) enacts such a superposition controlled on the state of a third quantum mode[16], however it inevitably results in tripartite entanglement of the target modes with the control mode. Instead, the exponential-SWAP (eSWAP) operation $U_E(\theta_C) = \exp(i\theta_C \text{SWAP}) = \cos(\theta_C) I + i\sin(\theta_C) \text{SWAP}$, where I is the identity operation, the SWAP gate fully exchanges the states of the two cavities and θ_C is the ancilla rotation (control) angle that provides

full tunability of the operation, directly enacts the superposition of gates while leaving the ancillary mode unentangled[6,17]. This operation is analogous to the exchange operation between two spins, where an interaction splits the symmetric and antisymmetric eigenstates and results in a dynamical exchange of the spin states in time[18–20]. The exchange operation provides an entangling gate for spins at particular interaction times and is the cornerstone of many schemes for universal quantum computation[21,22]. Similarly, at $\theta_C = \pi/4$, the eSWAP operation is essentially the $\sqrt{i\text{SWAP}}$ and deterministically entangles two bosonic modes, regardless of their encoding. This powerful feature allows quantum information processing with different bosonic codewords on the same hardware, making the eSWAP operation a valuable building block for universal quantum computation with bosonic modes[6].

Here, we devise an efficient circuit to implement the eSWAP operation in the 3D cQED architecture (detailed in Supplementary Information) and report the direct realization of the operation between two superconducting cavity modes controlled by a transmon ancilla. The original eSWAP protocol utilizes two quantum Fredkin gates[6], which are severely limited by ancilla decoherence. We implement a deterministic Fredkin gate in the same system, highlighting its vulnerability to the transmon decoherence that is reduced in our optimized eSWAP protocol. Using this operation, we demonstrate deterministic entanglement of the two cavity modes using Fock- and coherent-state encodings with a fidelity $F \approx 0.75$, without correcting for any state preparation and measurement (SPAM) errors. We then show full control over the unitary operation by varying the parameter θ_C. In particular, we highlight its action at the three primary settings of $\theta_C = \{0, \pi/4, \pi/2\}$, corresponding to the identity, entangling and full-SWAP operations, respectively. Finally, we perform full quantum process tomography (QPT) for these three operations, extracting a lower bound on the process fidelity of $F \approx 0.85$ for the {0,1} Fock encoding and $F \approx 0.60$ for the level-1 binomial encoding (Methods). Our results demonstrate the versatility of these operations as generalized entangling gates for universal quantum computation with bosonic modes.

Our system is designed to implement the eSWAP operation between states stored in two long-lived (milliseconds) bosonic quantum memories. In our system, two superconducting microwave cavities, Alice (orange) and Bob (blue), are dispersively coupled to a total of three transmons, as shown in Fig. 1a. The two transmons qA and qB, each coupled to a single cavity with strength χ_a and χ_b, respectively, are used for universal control and state-tomography of individual cavities[8,23]. A third, 'Y'-shaped transmon, qC, dispersively couples to both Alice and Bob[24]. The nonlinearity of its single Josephson junction enables four-wave mixing, which is used to enact a frequency-converting bilinear coupling with strength $|g|$ of the form $H_{BS}/\hbar = |g|(e^{-i\varphi}ab^\dagger + e^{i\varphi}a^\dagger b)$, where a $(a^\dagger)$ and b $(b^\dagger)$ are the annihilation (creation) operators for Alice and Bob, respectively, in the presence of two microwave drives with relative phase φ (Supplementary Information). Recent work has shown that this engineered coupling can be used to realize a robust beamsplitter and SWAP operation between two stationary bosonic modes[25].

[1]Department of Physics, Yale University, New Haven, CT, USA. [2]Department of Applied Physics, Yale University, New Haven, CT, USA. [3]Yale Quantum Institute, Yale University, New Haven, CT, USA. [4]These authors contributed equally: Yvonne Y. Gao, Brian J. Lester. *e-mail: yvonne_yuan_gao@imre.a-star.edu.sg; brianjlester@gmail.com; robert.schoelkopf@yale.edu
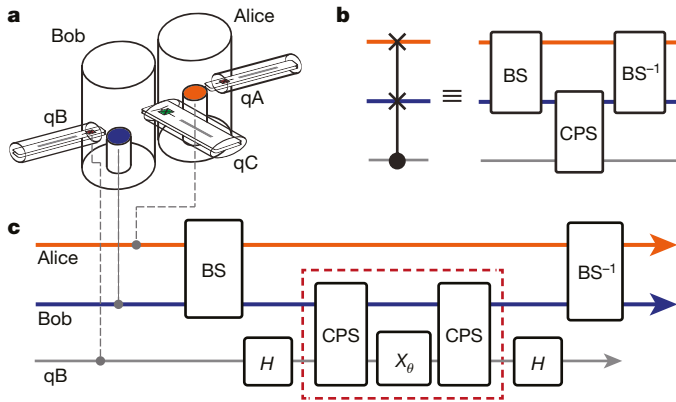
Fig. 1 | Sketch (not to scale) of device architecture and experimental protocol. a, The 3D cQED system used to realize the quantum Fredkin gate and eSWAP operations between two bosonic modes, Alice and Bob, and three transmon ancillae, qA, qB and qC. **b**, Decomposition of the Fredkin gate into two 50:50 beamsplitters (BS) and a controlled phase shift (CPS). The CPS is realized using the dispersive coupling between one of the cavity modes and a transmon ancilla, as described by the unitary $U_{CPS} = |g\rangle\langle g| \otimes I + |e\rangle\langle e| \otimes e^{i\pi n}$, where n is the photon number operator. **c**, Simplified circuit to realize the eSWAP unitary $U_E(\theta_C)$ between two bosonic modes controlled by an ancillary transmon, qB. The protocol consists of two BS operations separated by two Hadamard gates (H), two CPSs, and an ancilla rotation along the x axis, X_θ (see Supplementary Information).

Using this driven coupling, we realize a deterministic quantum Fredkin gate[16], where the states of Alice and Bob are swapped conditioned on the state of qB. Such a controlled-SWAP operation has only recently been demonstrated (non-deterministically) in linear optics experiments[26,27]. In our system, H_{BS} requires the satisfaction of the frequency-matching condition $|\omega_b - \omega_a| = |\omega_2 - \omega_1|$, where ω_a and ω_b are the frequencies of the cavities and ω_1 and ω_2 are those of the drives. When either Alice or Bob is dispersively coupled to a transmon ancilla with $|\chi_{a,b}| > |g|$, this process is intrinsically dependent on the state of the ancilla. We exploit this feature to perform a Fredkin gate on a selected set of initial states in the {0,1} Fock encoding (Extended Data Fig. 2). We estimate the quality of the operation to be ≥0.68, uncorrected for SPAM errors. A major source of imperfection is the transmon decoherence ($T_2 \approx 30\,\mu s$) because qB must remain in a coherent superposition during the entirety of the operation. We emphasize that implementing an eSWAP using two Fredkin gates and an ancillary control rotation, as proposed in ref. [6], would impose a strict limit to its performance.

Our implementation of the eSWAP operation ameliorates this penalty by minimizing both the total gate time and the duration over which the transmon is in a superposition. This is achieved by first decomposing the Fredkin gate into two 50:50 beamsplitters (BS) and a controlled phase shift (CPS) operation as shown in Fig. 1b. Because $U_{BS}^\dagger U_{BS} = I$, we eliminate two of the BS operations and reduce the total gate time (Supplementary Information). Additionally, we may commute the remaining two BS operations with the transmon rotations such that the final implementation, shown in Fig. 1c, keeps the ancilla in the ground state during the relatively slow BS operations. The CPS gates are realized using the dispersive coupling between qB and Bob, which imparts a π-phase to each photon in Bob when qB is excited for a period of $\sim\pi/\chi_b$. Therefore, we have effectively reduced the susceptibility to transmon relaxation, T_1, and dephasing, T_2, errors during the operation from $O[\gamma_t(t_{BS} + t_{CPS} + t_{rot})]$ to $O[\gamma_t(t_{CPS} + t_{rot})]$, where γ_t is the transmon decoherence rate and t_{BS} ($\sim5\,\mu s$), t_{CPS} ($\sim0.5\,\mu s$) and t_{rot} ($\sim50\,ns$) are the duration of the BS, CPS and transmon rotations, respectively. Furthermore, this implementation has the potential to be made tolerant of these errors by using higher levels of the transmon (S.M.G. and L.J.; manuscript in preparation).

The most useful feature of the eSWAP operation is the ability to entangle two bosonic modes regardless of their encoding. We demonstrate this by enacting the operation $U_E(\theta_C = \pi/4)$ on the input state
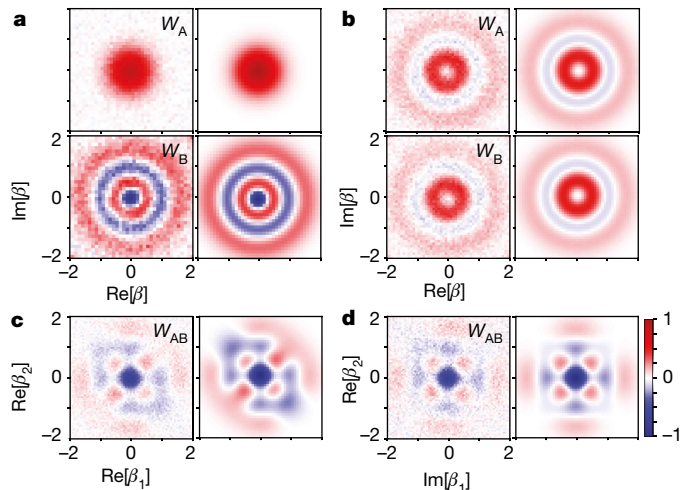

Fig. 2 | Deterministic entanglement in Fock encoding. a, The measured (left) and ideal (right) single Wigner functions of Alice (W_A; top) and Bob (W_B; bottom) after preparing $|0\rangle_A \otimes |3\rangle_B$. **b**, Left, the measured W_A (top) and W_B (bottom) after $U_E(\theta_C = \pi/4)$; right, the calculated ideal Wigner functions for a statistical mixture of $|0\rangle$ (top in **a**) and $|3\rangle$ (bottom in **a**). **c, d**, Left panels: the measured joint Wigner function (W_{AB}) after the operation $U_E(\theta_C = \pi/4)$ on Re–Re (**c**) and Re–Im (**d**) planes. Right panels: the ideal W_{AB} on the same planes for the maximally entangled state $\frac{1}{\sqrt{2}}(|0\rangle_A \otimes |3\rangle_B + i\,|3\rangle_A \otimes |0\rangle_B)$. Negativity at the origin indicates odd joint parity, which is preserved by the operation. Colour scale at lower right shows the value of the displaced parity.

$\Psi_{in} = |0\rangle_A \otimes |3\rangle_B$. We then perform Wigner tomography, omitting the normalization constant $\pi/2$, on Alice and Bob individually[23] to characterize their states before and after the operation (Fig. 2a, b). We observe that the initial (separable) state in each cavity has well-defined individual parity with $\langle P_A\rangle \approx +0.94$ and $\langle P_B\rangle \approx -0.9$. This indicates an odd joint parity with $\langle P_{AB}\rangle \approx -0.85$. We expect the final state after the operation to be a two-mode maximally entangled state $\Psi_{out} = \frac{1}{\sqrt{2}}(|0\rangle_A \otimes |3\rangle_B + i|3\rangle_A \otimes |0\rangle_B)$. The measured single-cavity Wigner functions suggest that the final states do not have a well-defined individual parity. This is an indication that after the operation, the joint cavity state is no longer separable and the independent measurements of each mode erases the coherence between them. Indeed, the measured Wigner functions of Alice, W_A, and Bob, W_B, show good agreement with the ideal case of a statistical mixture of $|0\rangle$ and $|3\rangle$.

In order to characterize the two-mode entangled state after the operation, we must consider the normalized joint Wigner function W_{AB} of Alice and Bob. We extract W_{AB} via shot-to-shot correlation of the photon number parity measurements of Alice and Bob after a displacement of β_1 and β_2, respectively (Methods)[24]. We present W_{AB} on the Re[β_1]–Re[β_2] and Re[β_2]–Im[β_1] planes in Fig. 2c, d, respectively. Our data (left panels of Fig. 2c, d) show excellent agreement with the ideal (right panels of Fig. 2c, d) for Ψ_{out}. The strong negativity at the origin indicates the preservation of negative joint parity by the entangling operation. The measured joint parity, $\langle P_{AB}\rangle \approx -0.75$ (uncorrected for SPAM errors) also provides a lower bound on the quality of the entangling operation (Methods).

Next, we highlight the codeword-independence of the eSWAP operation by investigating its action on Alice and Bob in the coherent state basis. To do so, we prepare the cavities in $\Psi_{in} \propto |-\alpha\rangle_A \otimes |\alpha\rangle_B$ (with $\alpha = 1.41$) and perform the eSWAP operation. In particular, we choose to focus on three primary instances, namely, the identity ($\theta_C = 0$), entangling ($\theta_C = \pi/4$), and full SWAP ($\theta_C = \pi/2$) operations. We expect that, for this choice of basis states, the Re–Re plane contains two positively valued Gaussian features that reveal the probability distribution of the coherent-state components. Correspondingly, the Im–Im plane contains interference fringes that indicate the quantum coherence, which is only present if the two cavity modes are entangled.
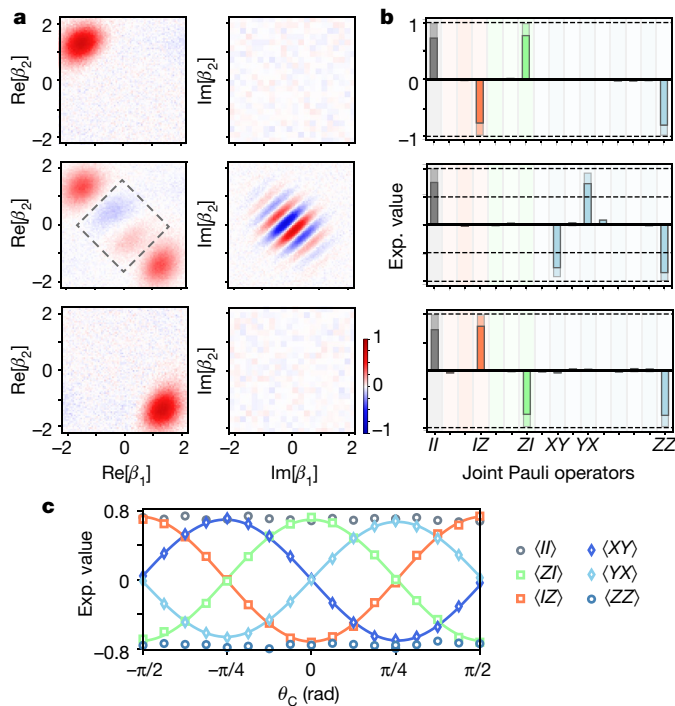
Fig. 3 | Characterization of eSWAP unitary in coherent state encoding.
a, The joint Wigner measurements in the Re–Re (left) and Im–Im (right) planes after $U_E(\theta_C = 0,\ \pi/4,\ \pi/2)$, respectively. For $\theta_C = 0$ (identity; top row) and $\theta_C = \pi/2$ (SWAP; bottom row), a single positively valued Gaussian feature is present on the Re–Re planes. With $\theta_C = \pi/4$ (middle row), interference fringes are present in the Im–Im plane, indicating deterministic entanglement creation. The additional features with non-zero displaced joint parity (within the dashed lines) in the Re–Re plane between the two main peaks can be accounted for by the self-Kerr nonlinearity of Alice and Bob. Measured values at the origin, which remain zero for all three operations, indicate the preservation of joint parity. The colour scale shows the value of the measured joint parity. **b**, The measured (solid bars) two-qubit Pauli operators for each of the processes. They show good agreement with the expected outcomes (transparent bars) for $\alpha \approx 1.41$. The ideal Pauli operators contain non-unity values for $\langle XY \rangle$ and $\langle YX \rangle$ due to non-orthogonality of the basis states at this chosen α. **c**, The expectation values of selected Pauli operators (see key) as we continuously vary the control angle, θ_C.

When $\theta_C = 0$, we observe that the population remains in the initial code-space, as shown by the location of the positively valued Gaussian features at $\mathrm{Re}[\beta_1] = -\alpha$ and $\mathrm{Re}[\beta_2] = +\alpha$. Conversely, when $\theta_C = \pi/2$, we see the coherent states are exchanged with $\mathrm{Re}[\beta_1] = +\alpha$ and $\mathrm{Re}[\beta_2] = -\alpha$. The absence of fringes in the Im–Im plane in both cases indicates that these operations do not result in any entanglement. Finally, we highlight that for the entangling operation, $\theta_C = \pi/4$, we observe an equal weight of each of the two coherent state components in the Re–Re plane. Further, we see the appearance of fringes in the Im–Im plane, which indicates the coherence between the two modes and signifies that we have generated a two-mode entangled cat state. Our results show excellent agreement with the ideal calculated joint Wigner functions, taking into account the self-Kerr nonlinearities of Alice and Bob (as discussed further in Supplementary Information).

The state of Alice and Bob can be considered as a pair of continuous-variable qubits encoded in the coherent state basis and can be fully characterized by measuring their two-qubit Pauli operators (correlators), each of which corresponds to one of the standard Pauli operators (I, X, Y, Z) applied to each qubit. Using the technique described in ref. [24], we do so efficiently by probing P_{AB} at 16 selected points of the phase space. The encoded two-qubit tomography after identity, entangling and SWAP are shown in Fig. 3b. For the case of identity and SWAP, we find exclusively single-qubit Pauli operators. In contrast, for the entangling case, only two-qubit operators are present, indicating strong non-classical correlations between the two modes. Based on this, we can evaluate a direct estimate of the fidelity to the

maximally entangled state[28] $\Psi_{AB} = \frac{1}{\sqrt{2}}(|-\alpha\rangle_A |\alpha\rangle_B + i|\alpha\rangle_A |-\alpha\rangle_B)$ of $\frac{1}{4}(\langle II \rangle + \langle XY \rangle + \langle YZ \rangle + \langle ZZ \rangle) \approx 74\%$. Additionally, we use the reconstructed logical density matrix (in the coherent state basis) to extract an average concurrence of $C \approx 0.65$ for $\theta_C = \pm\pi/4$, providing further verification of deterministic entanglement generated by the eSWAP operation.

Next, we demonstrate the full tunability of the eSWAP operation by probing a selected set of two-qubit Pauli operators as a function of θ_C (Fig. 3c). The measurement outcomes corresponding to $\langle II \rangle$, $\langle ZZ \rangle$ show no dependence of θ_C, indicating the preservation of photon numbers at all angles. Oscillations of $\langle IZ \rangle$, $\langle ZI \rangle$ are anti-correlated, consistent with the transfer of population between the modes. Finally, $\langle XY \rangle$ and $\langle YX \rangle$, which indicate two-qubit correlations, are exactly $\pi/4$ out of phase with $\langle IZ \rangle$ and $\langle ZI \rangle$ and show maximum contrast at $\theta_C = \pi/4$, where the single-qubit operators vanish. This is in good agreement with the expected signature of eSWAP and shows our ability to tune the operation via a single ancilla rotation, in analogy to varying the interaction time in an exchange gate.

Finally, we perform full QPT to obtain a quantitative analysis of our engineered operation. This is accomplished by applying the operation to 16 input states that together span the chosen code space and reconstruct the density matrices of the resulting states from their joint Wigner functions. We then construct the process matrices in the Pauli transfer representation[29] $R_E(\theta_C)$, which capture the action of the operation on any given set of input and output Pauli vectors, $P_{in,out}: P_{out} = R_E(\theta_C)P_{in}$. The measured and ideal $R_E(\theta_C)$ for Alice and Bob in the {0,1} Fock encoding are shown in Fig. 4a–c for the angles $\theta_C = \{0, \pi/4, \pi/2\}$, respectively. Our results show good qualitative agreement with the expected processes. From this, we can calculate a process fidelity of $F_E = (84 \pm 2)\%$ averaged over the three control angles, without correcting for SPAM errors. To estimate the non-idealities due to imperfect state preparation and measurement, we perform the same procedure for the process consisting of only the encoding and measurement. This yields a process fidelity of $F_{SPAM} = (88 \pm 2)\%$, suggesting that the measured F_E is probably limited by SPAM errors for this encoding. Additionally, we extract the concurrence when $\theta_C = \pm\pi/4$ as another quantitative measure of the entanglement created in the Fock encoding. This yields an average concurrence of $C \approx 0.66$ for the orthogonal input states $|0\rangle_A \otimes |1\rangle_B$ and $|1\rangle_A \otimes |0\rangle_B$, providing conclusive evidence of entanglement that is consistent with the uncorrected process fidelity computed above.

A crucial advantage of the eSWAP operation is its compatibility with error-correctable multi-photon encodings. To verify this capability, we perform QPT for the same three gates with both Alice and Bob encoded in the binomial basis[12]. The resulting process matrices again show good qualitative agreement with the expectation and we obtain an average $F_E \approx 60\%$ with an $F_{SPAM} = (77 \pm 2)\%$ (Methods). This indicates that our current implementation of eSWAP is more susceptible to errors when large photon number states are present in the cavity modes. We attribute this to three potential sources, namely, enhanced photon loss rate during the parametrically driven beamsplitter operations, self-Kerr nonlinearities of each mode, and the magnified susceptibility to small imperfections in the CPS gates. In general, the primary limitations arise from the strong parametric drives used to engineer the beamsplitter. It is possible to mitigate the associated imperfections by developing more sophisticated mixing elements. A detailed error budget is presented in Supplementary Information.

We have presented an efficient circuit for the eSWAP operation that can be adapted to any harmonic oscillator degrees of freedom coupled to nonlinear ancillae. We have demonstrated an experimental realization of the eSWAP between two bosonic modes in cQED and shown the deterministic entanglement of the state of two cavities encoded in Fock- and coherent-state bases. Together with single-mode gates, this provides a universal gate set on error-correctable qubits encoded in multi-photon states of cavities. Moreover, we may increase the number of cavities to implement the four-mode eSWAP gate, which will enable quantum information
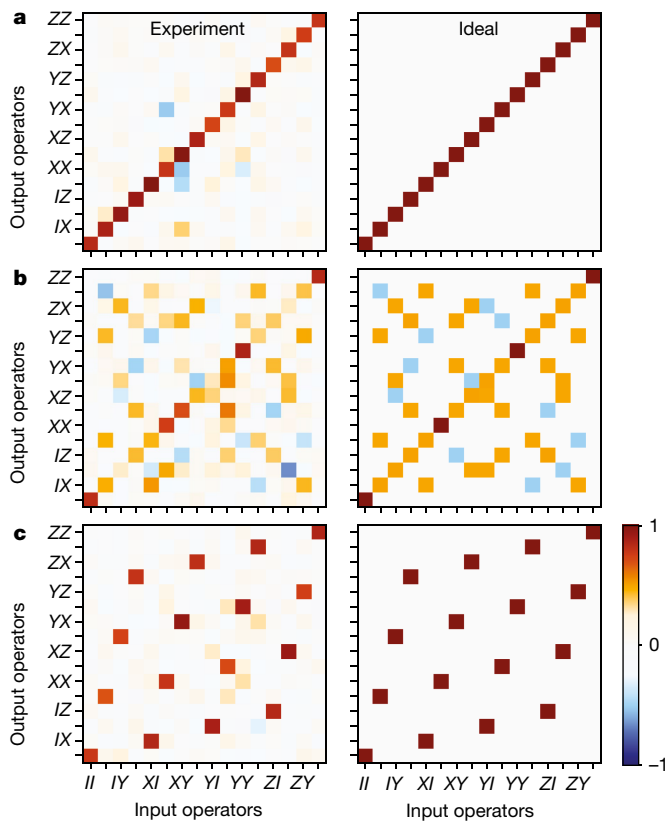
Fig. 4 | Quantum process tomography. a, The experimentally reconstructed (left) and ideal (right) quantum process tomography (QPT) of $U_E(0)$ in the $\{0,1\}$ Fock encoding. We represent the quantum process in the Pauli transfer representation (Methods). With all SPAM errors included, we obtain $F_0 \approx 86\%$. **b**, The reconstructed (left) and ideal (right) QPT of $U_E(\theta_C = \pi/4)$ with $F_{\pi/4} \approx 84\%$. **c**, The reconstructed (left) and ideal (right) QPT of $U_E(\theta_C = \pi/2)$ with $F_{\pi/2} \approx 83\%$. The colour scale shows the values for each element in the reconstructed process matrices.

processing with different bosonic encodings on the same hardware[6]. Our results also highlight the codeword-independent nature of the eSWAP operation. This enables us to exploit the strength of various bosonic encoding schemes within the same system and optimize the complexity for different local error models. The eSWAP operation provides both a key primitive for universal quantum computation using bosonic modes in cQED, as well as a powerful tool for the future implementation of quantum principal component analysis[30] and quantum machine learning[31].

Online content

Any methods, additional references, Nature Research reporting summaries, source data, statements of data availability and associated accession codes are available at https://doi.org/10.1038/s41586-019-0970-4.

1. DiVincenzo, D. P. The physical implementation of quantum computation. *Fortschr. Phys.* **48**, 771–783 (2000).
2. Nielsen, M. A. & Chuang, I. L. *Quantum Computation and Quantum Information* (Cambridge Univ. Press, Cambridge, 2000).
3. Chuang, I. L., Leung, D. W. & Yamamoto, Y. Bosonic quantum codes for amplitude damping. *Phys. Rev. A* **56**, 1114–1125 (1997).
4. Gottesman, D., Kitaev, A. & Preskill, J. Encoding a qubit in an oscillator. *Phys. Rev. A* **64**, 012310 (2001).
5. Sanders, B. C., Bartlett, S. D. & de Guise, H. From qubits to continuous-variable quantum computation. Preprint at http://arXiv.org/abs/quant-ph/0208008v1 (2002).
6. Lau, H.-K. & Plenio, M. B. Universal quantum computing with arbitrary continuous-variable encoding. *Phys. Rev. Lett.* **117**, 100501 (2016).
7. Reagor, M. et al. Quantum memory with millisecond coherence in circuit QED. *Phys. Rev. B* **94**, 014506 (2016).
8. Heeres, R. W. et al. Implementing a universal gate set on a logical qubit encoded in an oscillator. *Nat. Commun.* **8**, 94 (2017).
9. Ofek, N. et al. Extending the lifetime of a quantum bit with error correction in superconducting circuits. *Nature* **536**, 441–445 (2016).
10. Menicucci, N. C. et al. Universal quantum computation with continuous-variable cluster states. *Phys. Rev. Lett.* **97**, 110501 (2006).
11. Mirrahimi, M. et al. Dynamically protected cat-qubits: a new paradigm for universal quantum computation. *New J. Phys.* **16**, 045014 (2014).
12. Michael, M. H. et al. New class of quantum error-correcting codes for a bosonic mode. *Phys. Rev. X* **6**, 031006 (2016).
13. Albert, V. V. et al. Performance and structure of single-mode bosonic codes. *Phys. Rev. A* **97**, 032346 (2018).
14. Rosenblum, S. et al. A CNOT gate between multiphoton qubits encoded in two cavities. *Nat. Commun.* **9**, 652 (2018).
15. Chou, K. S. et al. Deterministic teleportation of a quantum gate between two logical qubits. *Nature* **561**, 368–373 (2018).
16. Milburn, G. J. Quantum optical Fredkin gate. *Phys. Rev. Lett.* **62**, 2124 (1989).
17. Filip, R. Overlap and entanglement-witness measurements. *Phys. Rev. A* **65**, 062320 (2002).
18. Petta, J. R. et al. Coherent manipulation of coupled electron spins in semiconductor quantum dots. *Science* **309**, 2180–2184 (2005).
19. Anderlini, M. et al. Controlled exchange interaction between pairs of neutral atoms in an optical lattice. *Nature* **448**, 452–456 (2007).
20. Kaufman, A. M. et al. Entangling two transportable neutral atoms via local spin exchange. *Nature* **527**, 208–211 (2015).
21. DiVincenzo, D. P., Bacon, D., Kempe, J., Burkard, G. & Whaley, K. B. Universal quantum computation with the exchange interaction. *Nature* **408**, 339–342 (2000).
22. Kempe, J., Bacon, D., Lidar, D. A. & Whaley, K. B. Theory of decoherence-free fault-tolerant universal quantum computation. *Phys. Rev. A* **63**, 042307 (2001).
23. Sun, L. et al. Tracking photon jumps with repeated quantum non-demolition parity measurements. *Nature* **511**, 444–448 (2014).
24. Wang, C. et al. A Schrödinger cat living in two boxes. *Science* **352**, 1087–1091 (2016).
25. Gao, Y. Y. et al. Programmable interference between two microwave quantum memories. *Phys. Rev. X* **8**, 021073 (2018).
26. Patel, R. B., Ho, J., Ferreyrol, F., Ralph, T. C. & Pryde, G. J. A quantum Fredkin gate. *Sci. Adv.* **2**, e1501531 (2016).
27. Ono, T., Okamoto, R., Tanida, M., Hofmann, H. F. & Takeuchi, S. Implementation of a quantum controlled-SWAP gate with photonic circuits. *Sci. Rep.* **7**, 45353 (2017).
28. Flammia, S. T. & Liu, Y.-K. Direct fidelity estimation from few Pauli measurements. *Phys. Rev. Lett.* **106**, 230501 (2011).
29. Chow, J. M. et al. Universal quantum gate set approaching fault-tolerant thresholds with superconducting qubits. *Phys. Rev. Lett.* **109**, 060501 (2012).
30. Lloyd, S., Mohseni, M. & Rebentrost, P. Quantum principal component analysis. *Nat. Phys.* **10**, 631–633 (2014).
31. Lau, H.-K., Pooser, R., Siopsis, G. & Weedbrook, C. Quantum machine learning over infinite dimensions. *Phys. Rev. Lett.* **118**, 080501 (2017).

Author contributions Y.Y.G. and B.J.L. fabricated the transmon qubits, assembled the experimental apparatus, and performed the experiments under the supervision of L.F., M.H.D. and R.J.S. Y.Y.G., B.J.L. and K.S.C. analysed the data. L.J. and S.M.G. provided theoretical support. Y.Y.G., B.J.L. and R.J.S. wrote the manuscript with feedback from all authors.

METHODS

Device architecture and system parameters. Our cQED system includes two three-dimensional (3D) superconducting microwave cavities, Alice and Bob, three transmon-type devices, and three quasiplanar readout resonators. All components are housed in a single block of high-purity (4N) aluminium in the structure shown in Extended Data Fig.1, which is chemically etched after machining to improve the surface quality. Alice and Bob act as quantum memories that are capable of coherently storing quantum information in bosonic states. They are formed by 3D coaxial transmission lines that are short-circuited at one end and open-circuited at the other by virtue of a narrow circular waveguide[7]. The resonance frequencies of the cavities' fundamental modes are determined by the lengths of the transmission lines (4.8 mm and 5.6 mm, respectively, for Alice and Bob).

An elliptical tunnel is machined between Alice and Bob, allowing the insertion of a chip containing a 'Y'-shaped transmon ancilla, qC, and its readout resonator into the cavities. Two additional tunnels are machined on either side of Alice and Bob to allow the incorporation of additional transmons, qA and qB, together with their respective readout channels. The superconducting transmons are fabricated on sapphire substrates using electron-beam lithography and a standard shadow-mask evaporation of Al/AlOx/Al Josephson junctions. During the same fabrication process, a separate strip of the tri-layer film is also deposited. Together with the wall of the tunnel, it forms a hybrid planar-3D $\lambda/2$ stripline resonator that is capacitively coupled to the transmon. This design combines the advantages of both precise, lithographic control of the critical dimensions and the low surface/radiation loss of 3D structures[32]. The chip containing these structures is inserted into the tunnel such that the transmon antenna(s) protrudes into the cavities to give the desired capacitive coupling to Alice and Bob. Each mode is coupled to the fridge input/output lines via standard SMA couplers.

This cQED system has eight bosonic modes: the two 3D cavities, three readout resonator and three transmon ancillae. Here we omit the readout modes for simplicity as they do not participate in the operation and are only involved during the file readout process. We label the two memories as modes A and B, while the three transmon modes are denoted by numerical subscripts with $j = 1, 2, 3$ corresponding to qA, qB, and qC, respectively. The transmons can be understood as LC oscillators with much larger anharmonicity compared with the other modes and they interact with the harmonic oscillator modes via standard dispersive coupling. Here, we also neglect the small residual dispersive coupling (<100 Hz) between Alice and qB, as well as that between Bob and qB. The cavity/resonator modes are modelled as near-harmonic oscillators with weak nonlinearity inherited from coupling to the Josephson junction. The system Hamiltonian can then be written in the following form up to the fourth order in the coupling of the memories to the transmons:

$$
\begin{aligned}
\frac{H}{\hbar} = {} & \omega_A \left(a^\dagger a + \frac{1}{2} \right) + \omega_B \left(b^\dagger b + \frac{1}{2} \right) \\
& + \sum_{j=1,2,3} \omega_j^{ge} |e\rangle_j |e\rangle_j - \chi_{A1}^{ge} a^\dagger a |e\rangle_1 |e\rangle_1 - \chi_{B2}^{ge} b^\dagger b |e\rangle_2 |e\rangle_2 \\
& - \chi_{A3}^{ge} a^\dagger a |e\rangle_3 |e\rangle_3 - \chi_{B3}^{ge} b^\dagger b |e\rangle_3 |e\rangle_3 - \frac{K_A}{2} a^\dagger a^\dagger a a \\
& - \frac{K_B}{2} b^\dagger b^\dagger b b - K_{AB} a^\dagger a b^\dagger b
\end{aligned}
\tag{1}
$$

The first two rows represent the excitation energy of the memory and transmon modes. The next row contains the second order terms representing the dispersive interactions (χ's) between the transmons and memories they couple to. The last row is the fourth order terms, including the self-Kerr energies (for example, K_A, K_B) of the resonators and the cross-Kerr interactions between any pairs of resonators (for example, K_{AB}). The parameters of all relevant components are summarized in Extended Data Table 1.

This system is an extension of the devices used in refs [24,25]. An additional ancilla with an independent readout resonator couples to each cavity in order to provide fast, independent cavity manipulations and tomography. In this case, qB also serves as the ancillary mode that controls the eSWAP operation angle. Crucially, the incorporation of the additional ancilla and readout modes enable us to perform simultaneous readout of each memory and obtain the joint Wigner tomography without involving additional levels in qC. This does not only remove the stringent parameter constraint on qC, as described in ref. [24], but also allows us to optimize the design of qC solely as the mixing element to enact the frequency-converting bilinear coupling between Alice and Bob[25]. This plays an important part in ensuring that the beamsplitter (BS) operations can be performed over a short duration without introducing non-idealities to the memory states significantly. We also characterize the coherence of each component in the system using standard cQED measurements. The results are summarized in Extended Data Table 2.

Joint Wigner tomography and state reconstruction. We characterize the collective state of Alice and Bob by probing their joint Wigner function, which, after

rescaling by $\pi^2/4$, is equal to the expectation value of their displaced joint photon number parity, $\langle P_J(\beta_1, \beta_2) \rangle$, in a four-dimensional phase space spanned by the complex numbers β_1 and β_2. In ref. [24], measurements of the joint parity, and thus, the scaled joint Wigner function, W_{AB}, were performed using the 'Y'-shaped transmon, qC, that dispersively couples to both Alice and Bob. This relies on using multiple-levels of qC to achieve an effective matched coupling strength to each cavity mode, which requires a relatively stringent set of system parameters.

In our system, the availability of the two ancilla, qA and qB, and their independent single-shot readout enables a simpler joint Wigner measurement. We simultaneously map the parity of Alice and Bob to their respective ancilla and perform joint single-shot readout on qA and qB. This yields the individual displaced parity $P_A(\beta_1)$ and $P_B(\beta_2)$. We then extract the joint displaced parity $P_{AB}(\beta_1, \beta_2) = P_A(\beta_1)P_B(\beta_2)$ by multiplying the two individual measurement outcomes in each run of the experiment. From this, we obtain the four-dimensional two-mode Wigner function $W_{AB} = \langle P_{AB}(\beta_1, \beta_2) \rangle$, which fully characterizes the joint state of Alice and Bob up to the cutoff number of photons, N_{cutoff}, which is chosen based on specific encoding. From this, we can reconstruct the density matrix ρ_{AB} in the restricted Hilbert space using standard techniques[24].

We do not constrain the trace of the extracted density matrix to be unity to avoid making any a priori assumptions about the different sources of imperfection. Failures of the state preparation, tomography and the operation will all manifest as a reduced trace and final state fidelity. For the $\{0,1\}$ Fock state encoding, we obtain an average state fidelity across the 16 basis states of ~85% with the operation and ~88% without. This provides an estimate of the reduction in state fidelity purely due to the state preparation and measurement imperfections. Additionally, we can infer the non-idealities due to the joint Wigner tomography by considering the state $|0\rangle_A |0\rangle_B$. This yields a state fidelity of ~90%, consistent with the maximum contrast of the individual parity measurements of Alice (~0.95) and Bob (~0.95). This is limited by the readout errors (~2%), ancilla decoherence (~2%) and imperfections in the transmon rotation pulses (~1%).

Similar analysis is done for the binomial encoding, which has an average photon number $\bar{n} = 2$ in each mode. It yields an average fidelity of ~80% for the initial states without the eSWAP operations. This degradation is primarily due to the longer optimal control theory (OCT) pulses ($\bar{n}/\chi_{a,b} \approx 1$ μs) required to prepare the initial states[8], which would fail if the transmon dephases. Therefore, this process is limited by the T_2 of qA and qB, which are relatively low in this particular sample compared to typical transmons. This can be improved in future implementations with better shielding, vibration isolation, and more robust package designs.

Realization of a quantum control-SWAP (Fredkin) gate. We can perform a full SWAP operation between two bosonic modes using the parametrically driven bilinear coupling as discussed in ref. [25]. This engineered coupling is only resonant when the drives satisfy the frequency-matching conditions of the four-wave-mixing process. Here, this is given by $\omega_2 - \omega_1 = \omega_b - \omega_a$, where ω_1 and ω_2 are the frequencies of the two drives and ω_a and ω_b are the frequencies of Alice and Bob, respectively. In our setup, Bob is dispersively coupled to qB, with strength χ_b. When $|\chi_b| \gg |g|$, where g is the bilinear coupling coefficient, the four-wave-mixing process can be tuned in and out of resonance by the state of qB.

To verify that this condition is sufficiently satisfied, we perform a spectroscopy experiment with qB initialized in $|+\rangle = (|g\rangle + |e\rangle)/\sqrt{2}$ and the cavities in $|0\rangle_A \otimes |1\rangle_B$. We then selectively excited qB conditioned on Bob being in vacuum as a function of the frequency and duration of one of the two drives with that of the other fixed as a chosen set of drive amplitudes. The results of this calibration experiment are shown in Extended Data Fig. 2a, where the colour bar corresponds to the probability of qB being measured in $|e\rangle$ after the final transmon rotation pulse. This provides an indication for the successful exchange of the single excitation between Alice and Bob, and hence, acts as a meter for whether the resonance condition for the bilinear coupling is satisfied. We observe that the SWAP operation is enacted at the frequencies ω and $\omega + \chi'$, which are well-separated compared to the spectral width of the resonance. We exploit this feature to realize the controlled-SWAP operation between Alice and Bob, using qB as the control mode. More specifically, we choose to position the drive frequency at ω, such that the bilinear coupling is resonant when qB is in $|e\rangle$. The resulting operation is described by:

$$
\text{cSWAP} = |g\rangle\langle g| \otimes I + |e\rangle\langle e| \otimes \text{SWAP}
\tag{2}
$$

This is a three-mode controlled-SWAP operation, also known as the quantum Fredkin gate[16]. Other protocols for the implementation of such an operation have been proposed in the context of quantum optics[33,34]. In contrast to the probabilistic nature of these protocols, our realization of the quantum Fredkin gate is fully deterministic. It produces a three-mode entangled state between Alice, Bob and qB when qB is initialized in a superposition state $|+\rangle$. We characterize the action of this operation on a set of four initial states by implementing conditional state tomography. This is an extension of the method used in ref. [35]. We perform a first measurement to detect the state of qB along one of its basis vectors $\{X, Y, Z\}$.

Subsequently, we perform a joint Wigner measurement[24] of Alice and Bob to extract their joint density matrix, ρ_{AB}. Finally, we construct the full three-mode density matrix, ρ, using a method described in ref. [2]:

$$\rho = \begin{pmatrix} \rho_1 & \rho_2 \\ \rho_3 & \rho_4 \end{pmatrix} \qquad (3)$$

where each of the constituent parts is given by the correlated transmon and cavity density matrices, with

$$\rho_1 = \mathcal{E}(|g\rangle\langle g|) \qquad (4)$$

$$\rho_4 = \mathcal{E}(|e\rangle\langle e|) \qquad (5)$$

$$\rho_2 = \mathcal{E}(|+\rangle\langle +|) - i\mathcal{E}(|-\rangle\langle -|) - (1-i)(\rho_1 + \rho_4)/2 \qquad (6)$$

$$\rho_3 = \mathcal{E}(|+\rangle\langle +|) + i\mathcal{E}(|-\rangle\langle -|) - (1+i)(\rho_1 + \rho_4)/2 \qquad (7)$$

where $\mathcal{E}(|k\rangle\langle k|)$ corresponds to the extracted ρ_{AB} after projecting into the transmon state $|k\rangle$. Using this technique, we obtain the density matrices shown in Extended Data Fig. 2b for the initial states $|g\rangle \otimes |0\rangle \otimes |1\rangle$, $|e\rangle \otimes |0\rangle \otimes |1\rangle$, $|+\rangle \otimes |0\rangle \otimes |1\rangle$ and $|-\rangle \otimes |0\rangle \otimes |1\rangle$, respectively. They are in good qualitative agreement with the expected density matrices, with an average overlap with ρ_{ideal} of $(68 \pm 5)\%$, without correcting for any SPAM errors. In particular, the bottom two plots show clear evidence of entanglement between the three modes with phases consistent with that of the initial superposition of qB.

To the best of our knowledge, this is the first experimental realization of a deterministic quantum Fredkin gate in cQED. It is a valuable tool for the implementation of universal quantum computation[36], quantum cyptography[37] and measurement[34].

Process χ-matrix analysis. In the main text and the analysis in the following section, we have chosen to represent the quantum process using the Pauli-transfer matrix representation R. This is a convenient choice for the representation of a general quantum process because it is a single real-valued matrix containing complete information[29]. However, another common representation is to reconstruct the state transfer matrix[38] χ. For general quantum processes, χ is a matrix of complex numbers, which is an over-complete representation of the process. Regardless, following the procedure described in ref. [38], we have analysed the same process data to construct χ matrices for each operation. The reconstructed χ matrices for the Fock encoding are shown in Extended Data Fig. 3. We obtain an average process fidelity $F = \text{tr}(\chi_i \chi_m)$ of the identity operation for state preparation (and no other operations) of $F \approx 0.85$. The process fidelities for the eSWAP operation are 0.88, 0.82 and 0.82, for the operational angles $\theta_C = 0$, $\pi/4$ and $\pi/2$, respectively. These are consistent with the analysis based on the Pauli-transfer matrices. Because both process representations are complete, we choose to focus our analysis on R representation for convenience.

The differences in the fidelity calculated using the χ representation and the R representation of the process is probably due to the combination of statistical uncertainty and the difference in how errors propagate in the different representations. As one example, the identity process in the χ representation is a complex matrix with only one entry, whereas in the R representation it is a diagonal matrix. This difference could lead to increased sensitivity to statistical fluctuations in the case of the χ representation (by weighting only a single element very heavily and removing the effects of all other entries).

Quantum error correction codes. We perform QPT, using same protocol described in the main text, on the three primary eSWAP operations with Alice and Bob encoded in the level-1 binomial code basis states[12]. We show the extracted Pauli transfer matrices for $\theta_C = 0$, $\pi/4$ and $\pi/2$ in Extended Data Fig. 4 left, middle and right, respectively. They show good qualitative agreement with the ideal processes but suffer a sizable reduction in contrast. We estimate the process fidelity by performing an overlap calculation of the measured $R_E(\theta)$ with the ideal cases.

This yields $F_0 \approx 0.7$, $F_{\pi/4} \approx 0.58$ and $F_{\pi/2} \approx 0.65$, with a fidelity of encoding of $F_{SPAM} \approx 0.77$.

Our results demonstrate that the eSWAP operation is indeed compatible with multi-photon quantum error correction (QEC) codes. Such bosonic encodings capitalize on the large available Hilbert space of a single harmonic oscillator to enable hardware efficient QEC, which has recently been successfully demonstrated for both the cat code[9] and binomial code[39]. The Gottesman, Kitaev and Preskill (GKP)[4] encoding is a more well-known example of continuous-variable bosonic encodings, but its creation is experimentally challenging. Such a state has only very recently been demonstrated for the first time using trapped ions[40]. Therefore, although the GKP encoding is perfectly compatible with the eSWAP operation implemented here, the demonstration of its action on such states is beyond the scope of this work. Additionally, several protocols have demonstrated the generation of entanglement between bosonic modes, which could potentially be extended to utilize error-correctable codeword states[41–43].

While our implementation of the code-independent entangling operation is a crucial primitive for realizing universal quantum computation using such error-corrected bosonic qubits, its fidelity deteriorates in the presence of large photon numbers in Alice and Bob. This is due to enhanced incoherent loss channels, such as photon jump and dephasing, as well as coherent errors, such as the self-Kerr nonlinearities of the cavity modes (a detailed error budget is present in Supplementary Information). According to the analysis done in ref. [13], the performances of the cat, binomial and GKP codes are comparable in mitigating the incoherent errors for a given mean photon occupation number $\bar{n}_{code} \approx 2$, with the GKP code having a slight advantage at low error rates. However, for the same $\bar{n}_{code}$, the GKP encoding is geometrically (that is, thermally) distributed and thus has a much larger tail in Fock space. This makes it more susceptible to the coherent errors arising from the self-Kerr of each cavity mode which are not accounted for by the current QEC protocols. Therefore, the choice of continuous-variable encodings must be based on the specific local error models and system parameters. This again highlights the importance of the code-independent nature of the entangling operation, which provides flexibility to optimize and change encodings on the fly.

Data availability

The data that support the findings of this study are available from the corresponding authors on reasonable request.

32. Axline, C. et al. An architecture for integrating planar and 3D cQED devices. *Appl. Phys. Lett.* **109**, 042601 (2016).
33. Gong, Y.-X., Guo, G.-C. & Ralph, T. C. Methods for a linear optical quantum Fredkin gate. *Phys. Rev. A* **78**, 012305 (2008).
34. Fiurášek, J., Dušek, M. & Filip, R. Universal measurement apparatus controlled by quantum software. *Phys. Rev. Lett.* **89**, 190401 (2002).
35. Vlastakis, B. M. et al. Characterizing entanglement of an artificial atom and a cavity cat state with Bell's inequality. *Nat. Commun.* **6**, 8970 (2015).
36. Lanyon, B. P. et al. Experimental demonstration of a compiled version of Shor's algorithm with quantum entanglement. *Phys. Rev. Lett.* **99**, 250505 (2007).
37. Ekert, A. K. et al. Direct estimations of linear and nonlinear functionals of a quantum state. *Phys. Rev. Lett.* **88**, 217901 (2002).
38. Chuang, I. L. & Nielsen, M. A. Prescription for experimental determination of the dynamics of a quantum black box. *J. Mod. Opt.* **44**, 2455–2467 (1997).
39. Hu, L. et al. Demonstration of quantum error correction and universal gate set on a binomial bosonic logical qubit. Preprint at http://arXiv.org/abs/1805.09072 (2018).
40. Flühmann, C. et al. Encoding a qubit in a trapped-ion mechanical oscillator. *Nature* https://doi.org (2018).please provide doi of linked Phys Lett when known.
41. Lähteenmäki, P., Paraoanu, G. S., Hassel, J. & Hakonen, P. J. Coherence and multimode correlations from vacuum fluctuations in a microwave superconducting cavity. *Nat. Commun.* **7**, 12548 (2016).
42. Pierre, M., Sathyamoorthy, S. R., Svensson, I., Johansson, G. & Delsing, P. Resonant and off resonant microwave signal manipulations in coupled superconducting resonators. Preprint at http://arXiv.org/abs/1802.09034 (2018).
43. Sandbo Chang, C. W. et al. Generating multimode entangled microwaves with a superconducting parametric cavity. *Phys. Rev. Appl.* **10**, 044019 (2018).
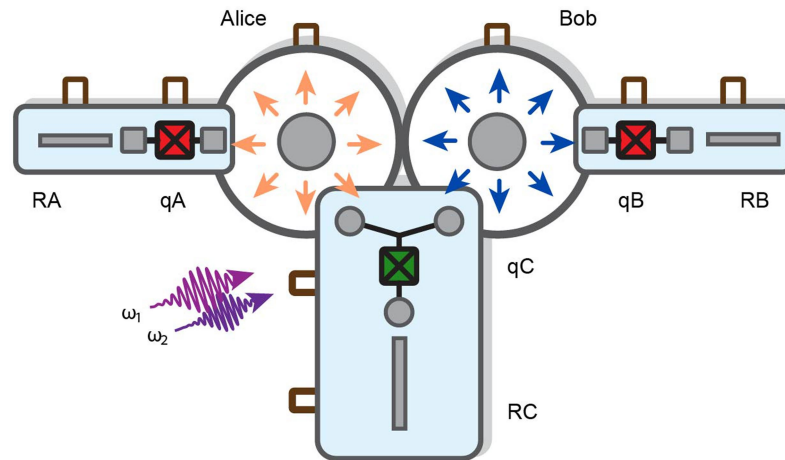
Extended Data Fig. 1 | Top view of the 3D double-cavity cQED system. The centre transmon ancilla (qC) provides nonlinear coupling between the modes of Alice (orange) and Bob (blue). The package accommodates two additional transmon ancillae, qA and qB, which are each coupled to one of the cavities Alice and Bob, respectively. Each transmon ancilla is measured via a neighbouring readout resonator (RA, RB, RC). The RF drives (ω_1, ω_2) are coupled to the system through the drive port of qC. See Methods for details.
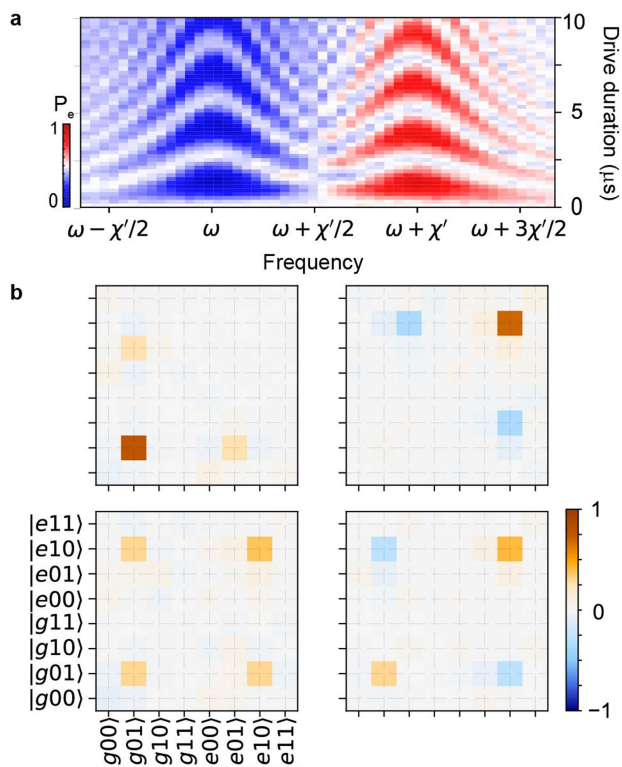
Extended Data Fig. 2 | A quantum Fredkin gate. a, The resonance condition for a parametrically driven SWAP operation measured as a function of one of the drive frequencies and the drive duration with the ancillary transmon initialized in $(|g\rangle + |e\rangle)/\sqrt{2}$. The colour scale shows the probability for the ancilla to be excited (P_e) after a rotation that follows the parametric drive. **b**, The reconstructed three-mode density matrix after the Fredkin gate for the initial states $|g\rangle \otimes |0\rangle \otimes |1\rangle$ (upper left), $|e\rangle \otimes |0\rangle \otimes |1\rangle$ (upper right), $\frac{1}{\sqrt{2}}(|g\rangle + |e\rangle) \otimes |0\rangle \otimes |1\rangle$ (bottom left) and $\frac{1}{\sqrt{2}}(|g\rangle - |e\rangle) \otimes |0\rangle \otimes |1\rangle$ (bottom right). The colour scale shows the real value of each element in the reconstructed density matrices.
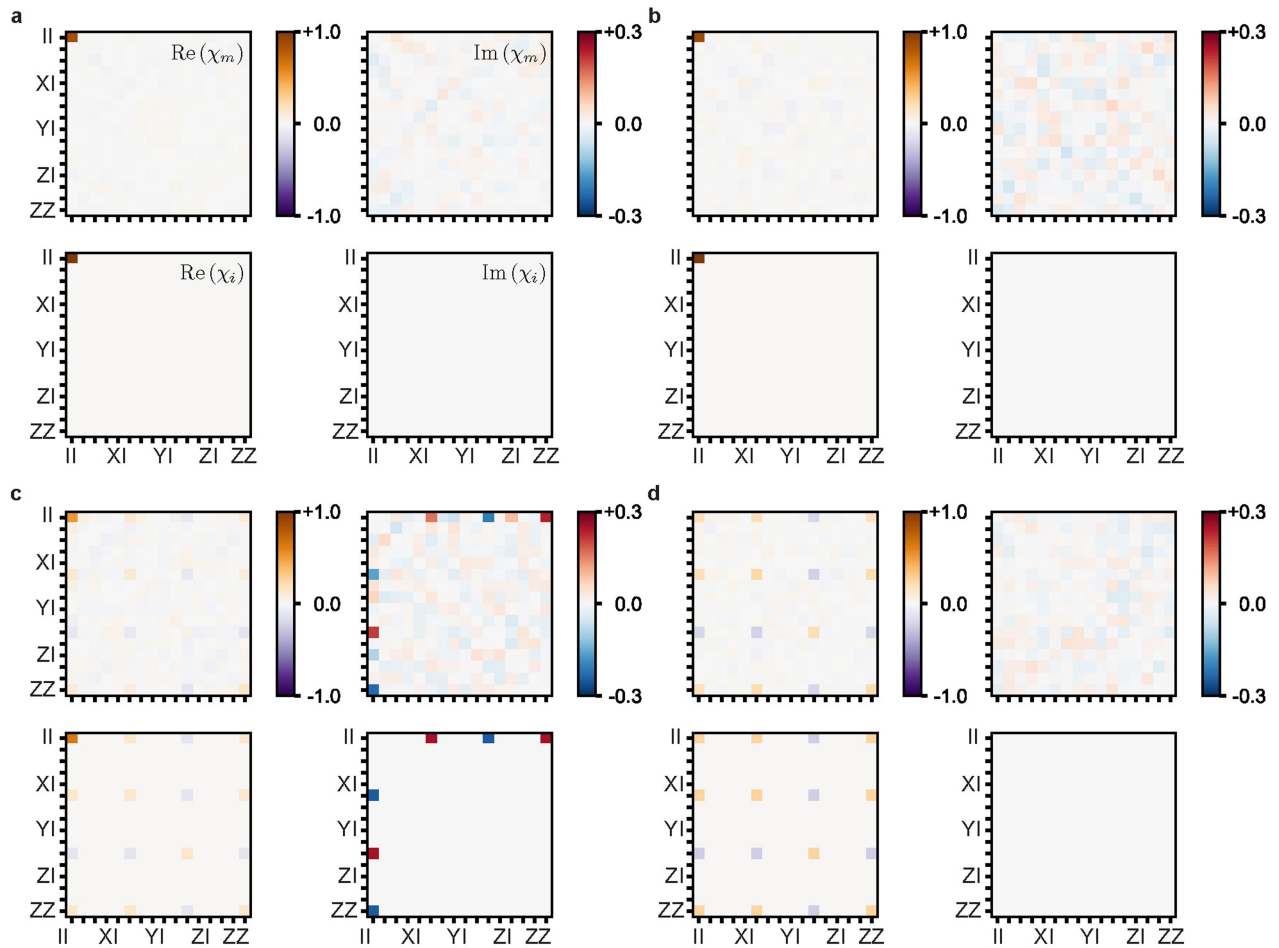
Extended Data Fig. 3 | The quantum process matrix for Fock encoding. The real (left) and imaginary (right) components of the complex process matrix χ are shown for the input (**a**), the identity operation (**b**), $\sqrt{\text{SWAP}}$ (**c**) and SWAP (**d**). For each operation, we show the measured (top) and ideal (bottom) matrices for comparison. Each of the measured process matrices are calculated without correction for SPAM errors. The colour scale shows the value for each (real or imaginary) component of the respective process matrices.
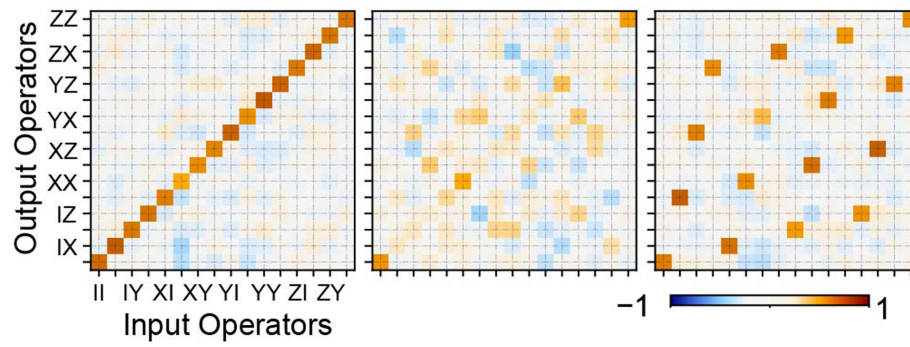
Extended Data Fig. 4 | QPT for binomial code. Left to right: the process matrix in the Pauli transfer representation for $U_E(0)$, $U_E(\pi/4)$ and $U_E(\pi/2)$ acting on Alice and Bob, encoded in the binomial basis. From these results, we obtain a process fidelity of 0.70, 0.58 and 0.65 for the three operations without correction for SPAM errors. The colour scale shows the value for each element of the respective process matrices.

Extended Data Table 1 | Hamiltonian parameters of all cQED components

Element	Frequency $\omega/2\pi$ (MHz)	Nonlinearity to element: $\chi_{ij}/2\pi$ (MHz)				
		Alice	Bob	qA	qB	qC
Alice	5467.25	$\lesssim 0.005$	—	0.79	—	0.37
Bob	6548.18	—	$\lesssim 0.005$	—	1.26	0.30
qA	4602.56	0.79	—	174.20	—	—
qB	4944.66	—	1.26	—	178.34	—
qC	5985.56	0.37	0.30	—	—	71.25
RA	7724.58	—	—	~ 1	—	—
RB	7722.30	—	—	—	~ 1	—
RC	8062.70	—	—	—	—	~ 1

Values that are within parentheses are estimated/simulated parameters. Some nonlinear couplings, such as χ between qA and Bob, are omitted because they are too small to be simulated or measured. The frequencies and couplings to the readout resonators (RA, RB and RC) are included for reference. The Hamiltonian is given in Methods (equation (1)).

Extended Data Table 2 | Coherence properties of the system

Element	T1 (μs)	T2 (μs)	T2$_e$ (μs)	P_e
Alice	200-300	350-400	—	$\lesssim 0.01$
Bob	300-350	450-500	—	$\lesssim 0.01$
qA	45-55	5-10	40-50	$\lesssim 0.02$
qB	70-80	25-35	75-85	$\lesssim 0.04$
qC	10-20	8-16	15-20	$\lesssim 0.01$

The device exhibits some fluctuations in its coherence times, but typical measured values for the relaxation (T_1), dephasing (T_2 and T_{2e}), and equilibrium excited state fraction (P_e) are given for each element in the system, when applicable. The coherence properties of Alice and Bob during the time of this experiment are inferior compared to those of the same device several thermal cycles ago ($T_1 \approx 1$ ms). This is probably a result of the degradation of its surface quality (through oxidation and thermal expansion/contraction cycles). We believe that the quality factors can be improved by chemically treating the surface of the cavities.